J. Plasma Phys. (2020), *vol.* 86, 815860303 © The Author(s), 2020.
Published by Cambridge University Press
doi:10.1017/S0022377820000422

Impacts of resonant magnetic perturbations on edge carbon transport and emission on EAST with EMC3-EIRENE modelling

S. Y. Dai[1,2,†], H. M. Zhang[3], B. Lyu[3,†], L. Wang[3], Y. Feng[4], Z. X. Wang[1] and D. Z. Wang[1]

[1]Key Laboratory of Materials Modification by Laser, Ion and Electron Beams (Ministry of Education), School of Physics, Dalian University of Technology, Dalian 116024, PR China

[2]DUT-BSU Joint Insititute, Dalian University of Technology, Dalian 116024, PR China

[3]Institute of Plasma Physics, Chinese Academy of Sciences, Hefei 230031, PR China

[4]Max-Planck-Institute für Plasmaphysik, D-17491 Greifswald, Germany

(Received 29 September 2019; revised 19 April 2020; accepted 20 April 2020)

The modelling of edge carbon transport and emission on EAST tokamak under resonant magnetic perturbation (RMP) fields has been conducted with the three-dimensional edge transport code EMC3-EIRENE. The measured vertical distribution of CVI emission by the extreme ultraviolet spectrometer system for the perturbed case shows a reduction in the CVI emission by 20 % compared to the equilibrium case. The chord-integrated CVI emission can be reconstructed by EMC3-EIRENE modelling, which presents an increase in the CVI emission with RMP fields. The discrepancy between experiments and simulations has been investigated by parameter study to examine the sensitivity of the simulation results on the edge plasma conditions and the impurity perpendicular transport. It is found that the variation of edge plasma conditions for the equilibrium case cannot resolve the discrepancy in the CVI emission between simulations and measurements. The simulations with enhanced impurity perpendicular transport coefficient allows a reasonable agreement with the measured reduction of CVI emission.

Key words: plasma simulation, fusion plasma

1. Introduction

The high-confinement mode (H-mode) with edge localized modes (ELMs) is recognized as the most likely operation regime for next-step tokamaks such as ITER (Loarte *et al.* 2007; Lang *et al.* 2013*a*; Loarte *et al.* 2014*a*,*b*). The intense particle and energy flux depositions on divertor targets induced by ELMs lead to material erosion, melting and vaporization (Federici *et al.* 2003; Eich *et al.* 2005; Bazylev *et al.* 2009; Rapp *et al.* 2009; 2011). Many ELM-control techniques have been proposed and developed for ELM mitigation and suppression on tokamak devices

---

† Email addresses for correspondence: daishuyu@dlut.edu.cn, blu@ipp.ac.cn

(Evans *et al.* 2013; Lang *et al.* 2013*b*). Resonant magnetic perturbation (RMP) application has been used on tokamaks as an effective technique to control ELMs (Evans *et al.* 2004; Burrell *et al.* 2005; Evans *et al.* 2006; Liang *et al.* 2007; Kirk *et al.* 2010; Suttrop *et al.* 2011; Jeon *et al.* 2012; Sun *et al.* 2016, 2017). However, tokamak devices with RMP application give rise to three-dimensional (3-D) effects on the edge plasma, i.e. the edge stochastization, which can change transport the characteristics of the edge plasma (Frerichs *et al.* 2012*a*,*b*; Lore *et al.* 2012; Lunt *et al.* 2012; Schmitz *et al.* 2014). Further, RMP-induced variation of edge magnetic topology leads to splitting of the divertor footprints of particle and heat fluxes, which might be beneficial for mitigation of peak value of power load on divertor targets (Schmitz *et al.* 2013; Frerichs *et al.* 2013, 2014, 2016*a*; Schmitz *et al.* 2016; Faitsch *et al.* 2017). In addition, experiments in the Large Helical Device (LHD) show that RMP fields change the edge impurity radiation location, which can be one possible reason for the triggering of detachment transition during RMP application (Kobayashi *et al.* 2010, 2013*a*).

The transport properties of edge impurities with and without RMP fields have been studied in LHD by the extreme ultraviolet (EUV) measurements of impurity emission (Zhang *et al.* 2017). However, impacts of the RMP fields on edge impurity transport on tokamaks are not well understood yet. The studies of the variation of edge impurity behaviours on tokamaks with and without RMP applications are imperative. Hence, investigations on the impacts of the perturbed fields on edge impurity transport and emission have been motivated, which have an important implication for the issues related to impurity screening and impurity content mitigation not only on present tokamak devices but also on ITER.

On EAST tokamak, the edge impurity transport and emission can be investigated based on a new development of an EUV spectrometer system (Shen *et al.* 2013; Vogel *et al.* 2018), which can provide the distributions of impurity emission in the edge region for the perturbed and equilibrium cases. In this study, the transport characteristics of the edge carbon impurity in the scrape-off layer (SOL) of EAST tokamak with and without RMP applications have been studied with the 3-D edge transport code EMC3-EIRENE (Feng *et al.* 2004; Reiter *et al.* 2005). The simulation results are compared with the EUV spectroscopic measurements of the CVI (33.7Å) emission for the cases with and without RMP fields. The EUV measurements show that the RMP application leads to a reduction in the CVI emission by 20 % compared to the unperturbed case. The carbon impurity distributions with different charge states are studied for the perturbed case by EMC3-EIRENE modelling. Reconstruction of the chord-integrated CVI emission from EUV measurements has been carried out by EMC3-EIRENE modelling, which shows the simulated CVI emission intensity is higher during RMP application than that without RMP fields. A parameter study of the edge plasma parameters and impurity perpendicular transport coefficient has been attempted to reproduce the observed reduction in the CVI emission during RMP application.

In § 2, the RMP coil system, time traces of selected discharge and measurements of CVI emission by the EUV spectrometer are briefly described. Section 3 gives a short introduction to the plasma and impurity transport models in the EMC3-EIRENE code. The studies of impurity transport and emission during RMP application are conducted in § 4, and the simulated CVI emission distribution is compared with the EUV measurements. In § 5, issues related to the simulated CVI emissions which are compared with the EUV spectroscopic measurements are discussed. Finally, the results are summarized in § 6.

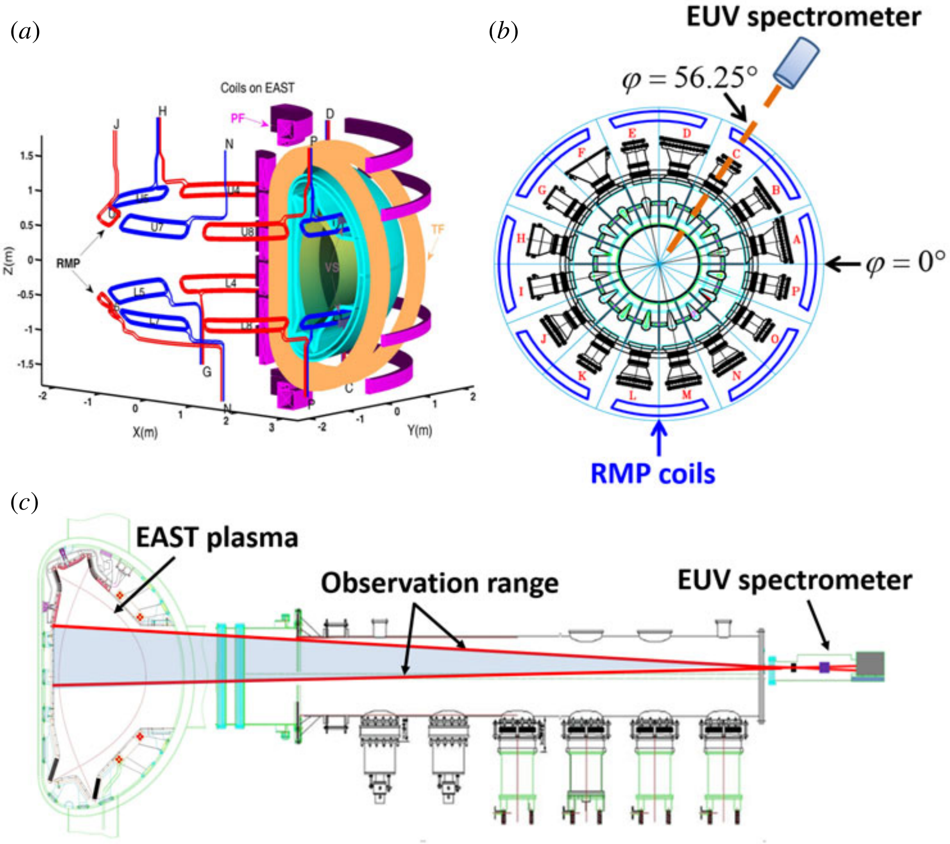

FIGURE 1. Three-dimensional schematic view of the RMP coil system (*a*), top view of toroidal locations of the EAST ports, EUV spectrometer and RMP coils (*b*) and schematic view of the EUV spectrometer system (*c*) on EAST.

2. Experiments on EAST

2.1. *RMP coil system*

Figure 1(*a*) shows the 3-D schematic view of the RMP coil system on EAST. The RMP coil system consists of 2 coil arrays with up–down symmetry structures. Each coil array has 8 coils uniformly distributed along the toroidal direction, and each coil has 4 turns. The maximum coil current is designed to be 10 kAt ($=2.5$ kAt × 4 coil turns). The toroidal mode number of the RMP generated by the coil system can be up to $n=4$ for static perturbations. There are 16 ports, denoted A to P, as shown in figure 1(*b*), which displays the top view of toroidal locations of the EAST ports and RMP coils. The middle location of the P and A ports is defined as $\varphi = 0^\circ$ in this work. Each RMP coil covers two ports in the toroidal direction. The current of the *k*th coil in an array is prescribed by $I_{\mathrm{k}} = A\cos(n\varphi_k - \varphi_0)$, where A is the amplitude, n is the toroidal mode number, φ_k is the toroidal angle of the *k*th coil centre and φ_0 is the phase of each array of coils; φ_0 is always referred to as current phases φ_U and φ_L for upper and lower coil arrays, respectively. A detailed introduction to the RMP coil system on EAST is given in Jia *et al.* (2016, 2018*a*,*b*). In this study, the edge carbon

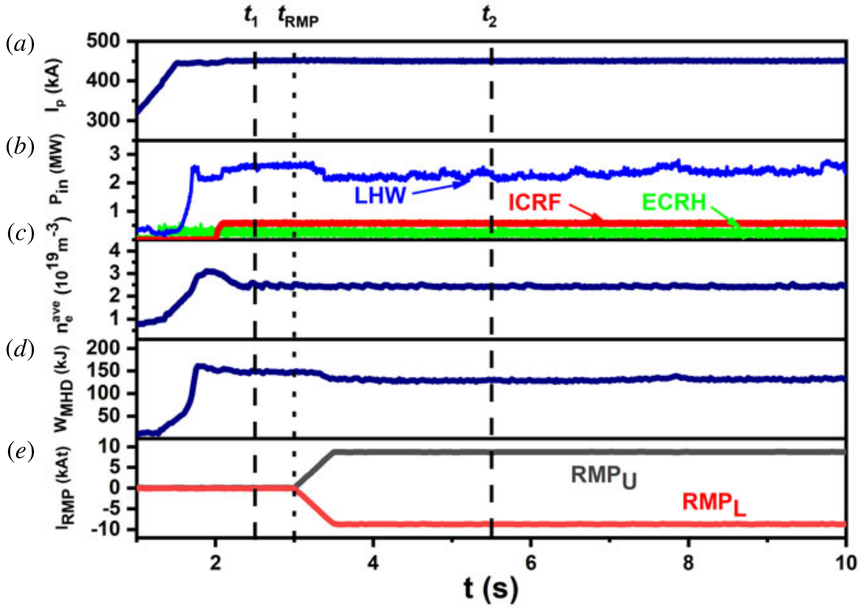

FIGURE 2. Time evolution of plasma current (*a*), injected power (*b*), line-averaged electron density (*c*), stored energy (*d*) and RMP coil currents for upper and lower arrays (*e*) for shot #67578.

transport behaviour during RMP application is studied for shot #67578 by using $n = 1$ RMP field ($A = 8.8$ kAt, $\varphi_U = 21^\circ$ and $\varphi_L = 158^\circ$). In addition, figure 1(*b*) also shows the toroidal position of the EUV spectrometer, which is located at C port with the toroidal angle of $\varphi = 56.25^\circ$.

2.2. *Measurements of the CVI emission*

Figure 1(*c*) displays a schematic of the EUV spectrometer system on EAST, which is installed at the outboard midplane port. The EUV spectrometer system on EAST is commonly used in the diagnostics of the edge impurity behaviour by observing the distribution of spectral intensity and the shape of impurity lines (Shen *et al.* 2013; Vogel *et al.* 2018). The EUV spectrometer mainly consists of an entrance slit, a varied line spacing groove grating and a charge coupled device. The time resolution of the EUV spectrometer is about 100 ms when the vertical profile is measured. A spatial resolution of 45 mm is achieved when the space-resolved slit width is set to 1 mm and 100 pixels of sensing surface are binned for a single channel. The horizontal position of the entrance slit is about 9.0 m away from the plasma centre at $R_{ax} = 1.75$ m. The vertical and toroidal observation ranges of the EUV spectrometer are around 50 and 8 cm, respectively. The working wavelength range of the EUV spectrometer is in the range from 3 to 50 nm. Detailed information about the EUV spectrometer used on EAST is introduced in Shen *et al.* (2013) and Vogel *et al.* (2018).

Figure 2 presents the time traces of the selected discharge (shot #67578 for H-mode) with a ∼20 s duration pulse. At the beginning of the discharge (before $t = 2$ s), the plasma is heated by the lower hybrid wave (LHW) with a power of ∼2.5 MW and electron cyclotron resonance heating with a power of ∼0.3 MW,

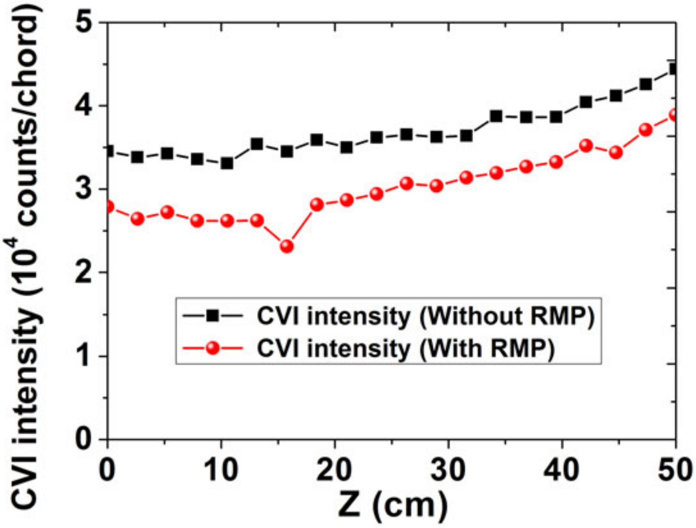

FIGURE 3. Profiles of the vertical distributions of CVI (33.7 Å) emission intensities measured by the EUV spectrometer for the cases with and without RMP applications.

respectively. Then, the plasma current (I_p) reaches a stable value of 450 kA. From $t = 2$ s, the ion cyclotron radio frequency heating is switched on with a heating power of ∼0.6 MW. The line-averaged electron density (n_e^{ave}) stabilizes at 2.4×10^{19} m^{-3} and the stored energy (W_{MHD}) is approximately 150 kJ. The RMP is applied from $t_{\mathrm{RMP}} = 3$ s (indicated by the vertical dotted line) and then the RMP coil current reaches a steady amplitude of 8.8 kAt for both upper and lower coil arrays. The application of RMP fields leads to a slight reduction in the LHW power and the stored energy, while other parameters are maintained the same. In this work, two timings ($t_1 = 2.5$ and $t_2 = 5.5$ s), indicated by the vertical dashed lines, are studied, which are referred to as the 'without RMP application' and 'with RMP application', respectively.

Figure 3 presents the vertical profiles of the chord-integrated CVI emissions (emitted by C^{5+}) measured by the EUV spectrometer at $t_1 = 2.5$ s (without RMP application) and $t_2 = 5.5$ s (with RMP application). The value of Z (horizontal axis) indicates the vertical position in the EUV observation range. Here, the value of $Z = 0$ cm indicates the position of the midplane. In addition, the upper X-point is located at $Z = 81.5$ cm. The CVI emission during RMP application reduces by 20 % compared to no RMP case. Further, it is found that the CVI emissions for both the perturbed and equilibrium cases increase along Z. This is due to a relatively long observation chord length as Z increases, which can be seen later in figure 7. In addition, other similar discharges (#67568 and #67574) with a shorter duration pulse (∼10 s) have been checked to confirm the response characteristics of the CVI emission under RMP application. It is found that the same phenomenon of reduced CVI emission after RMP application can be reproducible by the EUV spectrometer. Based on the above experimental results, the transport and emission behaviours of the carbon impurity during RMP application are studied by EMC3-EIRENE code, and efforts have been made to interpret the observed CVI reduction during RMP application.

3. The EMC3-EIRENE code

The EMC3-EIRENE code can well treat the plasma and impurity transport in an arbitrary 3-D magnetic configuration such as helical devices and non-axisymmetric tokamaks with RMP fields, which has been widely used for 3-D edge plasma modelling (Feng *et al.* 2017). The EMC3 code solves a reduced set of Braginskii fluid equations for the particle, momentum and energy transport of ions and electrons, and is self-consistently coupled with the EIRENE code to treat the transport of neutral atoms and molecules. The parallel transport along the magnetic field is assumed to be classical, while for the cross-field transport anomalous diffusion is assumed. The Monte Carlo (MC) method is employed to solve the fluid equations for the steady-state plasma temperature, density and parallel flow distributions. The magnetic field aligned grid is used by EMC3 to provide computationally effective access to fast magnetic field reconstruction during the MC particle tracing based on the reversible field line mapping technique (Feng *et al.* 2005; Frerichs *et al.* 2010). This magnetic geometry can well treat both open field lines that terminate on the target plates and closed field lines that exist inside the plasma core. In previous EMC3-EIRENE modelling on EAST (Huang *et al.* 2014; Xie *et al.* 2018*a*,*b*), the computational grids for the axisymmetric equilibrium fields have been constructed by the EFIT code (Lao 1990). The impacts of the perturbation fields are simulated by using the vacuum approach in this study (Frerichs *et al.* 2012*a*; Lore *et al.* 2012; Lunt *et al.* 2012), in which the vacuum perturbed fields are superimposed on the EFIT equilibrium field. The plasma response effects to the perturbation fields are not included in the current work (Lore *et al.* 2017).

The EMC3 code also includes a self-consistent treatment of impurity transport for the studies of the relevant impurities (Feng *et al.* 2002). The friction force and the ion thermal force are the dominant forces acting on the impurity according to Stangeby (2000). The balance between the friction force and the ion thermal force determines the transport of the impurity and thereby the impurity distribution in the edge plasma. Both the friction force and the ion thermal force are associated with the background plasma parameters, implying that the force balance can be affected by the background plasma conditions. The feedback of impurities on the background plasma is given by the energy sinks due to excitation and ionization of impurities. A sophisticated post-processing program for calculating the volumetric emissivity has been developed, which can trace the lines of sight for each observation chord of the EUV spectrometer through the 3-D emission distribution obtained from the EMC3-EIRENE code. This post-processing program based on EMC3-EIRENE simulations has been validated against spectral measurements of impurity emission in LHD (Dai *et al.* 2016*a*,*b*, 2018; Kawamura *et al.* 2018; Oishi *et al.* 2018). In addition, 3-D reconstruction of the spectroscopic measurements of the H_α and CIII emissions on Wendelstein 7-X has been performed as well based on the EMC3-EIRENE modelling (Frerichs *et al.* 2016*b*, 2017).

4. Modelling of the CVI emission

4.1. *Set-up of EMC3-EIRENE simulations*

The input parameters for EMC3-EIRENE modelling are specified according to the experimental measurements during EAST exposure (shot #67578). Two scenarios for different timings ($t = 2.5$ and 5.5 s) during the discharge are simulated in this work, which are used to calculate the CVI emission and to compare with the experimental data. The experiment is attempted for deuterium discharges with the toroidal magnetic field of $B_t = 2.48$ T. The magnetic configuration for shot #67578 is biased towards the upper single null (USN) magnetic configuration, while the computational grid is constructed as a disconnected double null magnetic configuration. Here, the disconnected double null magnetic configuration indicates that the main plasma in the generated grid is connected to the upper divertor and disconnected from the lower divertor. The computational grids for EMC3-EIRENE modelling are constructed according to the cases without RMP application at $t_1 = 2.5$ s and with RMP application at $t_2 = 5.5$ s. The toroidal simulation domain is covered by the complete 360° computational grid. The normalized poloidal magnetic flux ψ_N ($\approx$0.7) is used to define the inner radial boundary at the upstream. Here $\psi_N = (\psi - \psi_{ax})/(\psi_{sep} - \psi_{ax})$, where ψ_{ax} and ψ_{sep} are the poloidal magnetic fluxes at the axis and the separatrix, respectively. The respective boundary conditions for particle transport and energy transport are the upstream density (n_u) and input power (P_{SOL}) in the modelling, which are obtained experimentally. The absorbed input power is approximately $P_{SOL} = 2.3$ MW, which is injected through the inner radial boundary into the computational domain. The upstream density $n_u = 0.73 \times 10^{19}\ \mathrm{m}^{-3}$ at $\psi_N \approx 0.8$ is employed for the perturbed case while there are no available experimental data for the equilibrium case. In the modelling, $n_u = 0.73 \times 10^{19}\ \mathrm{m}^{-3}$ is tentatively used for the equilibrium case, whereas the impacts of the uncertainty in n_u are discussed in § 5. The Bohm sheath boundary condition is used at the divertor target plates. The ion and electron sheath heat transmission coefficients are assumed to be 2.5 and 4.5, respectively (Stangeby 2000). The upper and lower divertor target plates are made of tungsten and carbon materials on EAST, respectively. Since the sputtering yield of the tungsten material is much lower compared to the carbon material (Federici *et al.* 2001; Eckstein 2008), the individual sputtering coefficients are assumed to be 0.001 and 0.01 for tungsten and carbon targets in the modelling (Dai *et al.* 2015). The test modelling has shown that the energy exhausted by the tungsten impurity has a slight influence on the edge plasma parameters due to a small amount of eroded tungsten. Therefore, the tungsten impurity has a minor impact on the simulated carbon impurity emission distributions in this work. In addition, the small plasma-wetted area and eroded carbon amount at the lower divertor targets lead to a minor influence of carbon sputtering coefficient on the CVI emission intensity ratios defined later according to test simulation. Here, it should be noted that the same carbon sputtering coefficients for the equilibrium and perturbed cases are used in the modelling. The neutral impurity is released from the divertor target plates according to the plasma flux deposition distribution.

Figure 4 shows the 2-D distributions of the connection length (L_c) for the cases without and with RMP applications at the toroidal angle of $\varphi = 56.25°$. The L_c in the SOL region for no RMP fields is shorter than 200 m, as shown in figure 4(*a*). The application of RMP fields can break the original flux surfaces of the equilibrium fields, which results in the structure of the helical lobes in figure 4(*b*). The helical lobes are formed by the splitting of the unperturbed separatrix into multiple invariant manifolds (Evans *et al.* 2005). The Poincaré plot for the perturbed fields is also plotted in figure 4(*b*). It can be seen that a stochastic magnetic geometry is formed due to the application of RMP fields. Although the edge magnetic configuration becomes stochastic, the L_c (>1000 m) inside the perturbed separatrix is still much larger than that in the SOL region. In addition, it is also seen that large magnetic islands exist due to the application of RMP fields, which are located at $\psi_N = 0.85$–0.9. The stochasticity can lead to a more complex impurity transport behaviour according to the previous EMC3-EIRENE simulations in LHD (Kobayashi *et al.* 2008, 2009, 2013*b*, 2017, 2019; Dai *et al.* 2016*a*,*b*, 2018; Kawamura *et al.* 2018; Oishi *et al.* 2018). In this work,

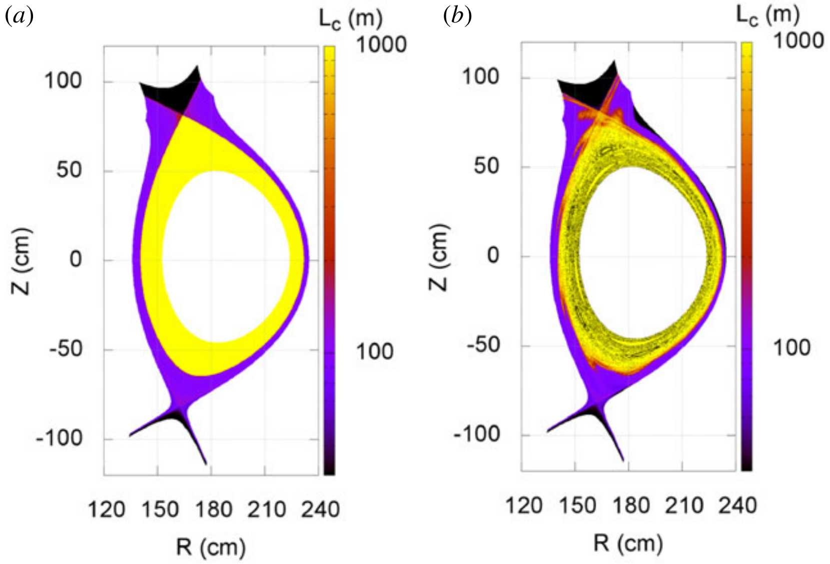

FIGURE 4. Two-dimensional distributions of the connection length for the cases without RMP (*a*) and with RMP (*b*) applications by EMC3-EIRENE modelling at the toroidal angle of $\varphi = 56.25^\circ$. The Poincaré plot for the perturbed fields is superimposed on the connection length distribution in figure 4(*b*).

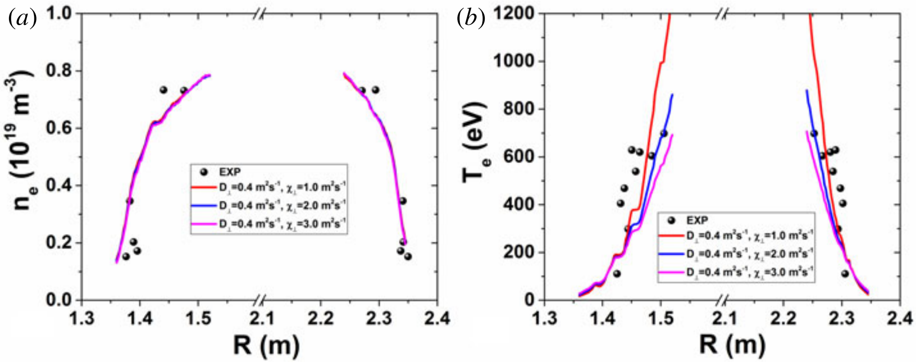

FIGURE 5. Horizontal profiles of the electron density (*a*) and temperature (*b*) in the experiments and simulations at the midplane of EAST for the perturbed case (shot #67578, $t_2 = 5.5$ s). A mapping of the electron density and temperature profiles at the inboard midplane has been performed according to the measurements at the outboard midplane.

we focus on the study of the variation of impurity transport characteristics induced by the RMP fields on EAST.

The cross-field particle and energy transport coefficients of the background plasma, $D_\perp$ and $\chi_\perp$, are determined by fitting the electron density and temperature profiles measured by the edge reciprocating probe on EAST. Figure 5 displays the electron density (n_e) and temperature (T_e) distributions measured at the midplane of EAST and modelled by EMC3-EIRENE under RMP application. The measurements of the n_e and T_e profiles are obtained by the reciprocating probe at the outboard midplane. The n_e and T_e profiles at the inboard midplane are mapped according to the measurements at the outboard midplane. It can be seen that the scattered T_e values measured by the reciprocating probe make it difficult to obtain a clear fit between simulation and experiment in figure 5(*b*). The simulated T_e profiles for $\chi_\perp = 3.0\ \mathrm{m^2\ s^{-1}}$ are lower than the measured data at the regions of $R > 1.45$ m and $R < 2.3$ m in figure 5(*b*). For $\chi_\perp = 1.0\ \mathrm{m^2\ s^{-1}}$, the modelled T_e profiles show a better match in the middle of the computational domains ($1.45 < R < 1.48$ m and $2.27 < R < 2.3$ m), whereas the modelled T_e values are much higher than the experimental data at the innermost regions ($R > 1.48$ m and $R < 2.27$ m). Therefore, the value of $\chi_\perp = 2.0\ \mathrm{m^2\ s^{-1}}$ is employed for the perturbed case. Moreover, the present set of $D_\perp = 0.4\ \mathrm{m^2\ s^{-1}}$ and $\chi_\perp = 2.0\ \mathrm{m^2\ s^{-1}}$ is consistent with the previous EMC3-EIRENE modelling on EAST (Huang *et al.* 2014). Henceforth, the use of $D_\perp = 0.4\ \mathrm{m^2\ s^{-1}}$ and $\chi_\perp = 2.0\ \mathrm{m^2\ s^{-1}}$ is fixed for the perturbed case in the modelling. Since there are no available experimental data for the equilibrium case, n_u, $D_\perp$ and $\chi_\perp$ are assumed to be the same as the RMP application case according to Lore *et al.* (2012), Lunt *et al.* (2012) and Frerichs *et al.* (2012*b*). In § 5, a parameter study has been performed to constrain the uncertainty of edge plasma conditions for the equilibrium case. The impurity perpendicular diffusivity D_{imp} is assumed to be the same as the background plasma, i.e. $0.4\ \mathrm{m^2\ s^{-1}}$ as a default value for carbon impurity unless stated otherwise. The above-mentioned parameters are used as the default values for the following EMC3-EIRENE simulations.

4.2. *Carbon impurity distribution with RMP application*

Figure 6 shows the 2-D distributions of $\mathrm{C^{1+}}$–$\mathrm{C^{6+}}$ ions by EMC3-EIRENE modelling with RMP application at the toroidal angle of $\varphi = 56.25^\circ$ where the EUV spectrometer is located. The plasma-wetted area is very small on the lower divertor targets due to the USN configuration used for shot #67578, which leads to a low incident plasma flux and eroded carbon flux. The $\mathrm{C^{1+}}$ and $\mathrm{C^{2+}}$ ions are mainly distributed at the lower divertor legs region in figure 6(*a*,*b*). The $\mathrm{C^{3+}}$ ions can penetrate deeper, which leads to an impurity build-up around the lower *X*-point region as shown in figure 6(*c*). For $\mathrm{C^{4+}}$–$\mathrm{C^{6+}}$ ions, it is seen that the penetration depth increases radially with the increase in the charge state of carbon impurity in figure 6(*d*–*f*). The $\mathrm{C^{4+}}$ ions are mainly in the SOL region and $\mathrm{C^{5+}}$–$\mathrm{C^{6+}}$ ions are inside the perturbed separatrix due to the high ionization potential. In the following subsection, the present study will focus on the transport behaviour of $\mathrm{C^{5+}}$ (CVI) under RMP fields to make a detailed comparison between the EUV observation and the EMC3-EIRENE simulation.

4.3. *Comparison between the simulation and the experiment*

Figure 7 shows the 2-D distribution of the CVI emission intensity by EMC3-EIRENE modelling with RMP application at the toroidal angle of $\varphi = 56.25^\circ$. The green dashed lines indicate the vertical observation range of the EUV spectrometer ($Z = 0$–50 cm). The CVI emission intensity is calculated by (4.1)

$$I^z\,(T_e, n_e) = n_e \cdot n^z_{imp} \cdot L^z\,(T_e)\,, \tag{4.1}$$

where n_e is the electron density, n_{imp} is the impurity density, z is the charge state of carbon impurity and $L^z(T_e)$ is the emission coefficient taken from ADAS database (open-ADAS database, http://open.adas.ac.uk/). The stronger CVI emission is obtained inside the perturbed separatrix in figure 7. According to the results in figure 4(*b*),

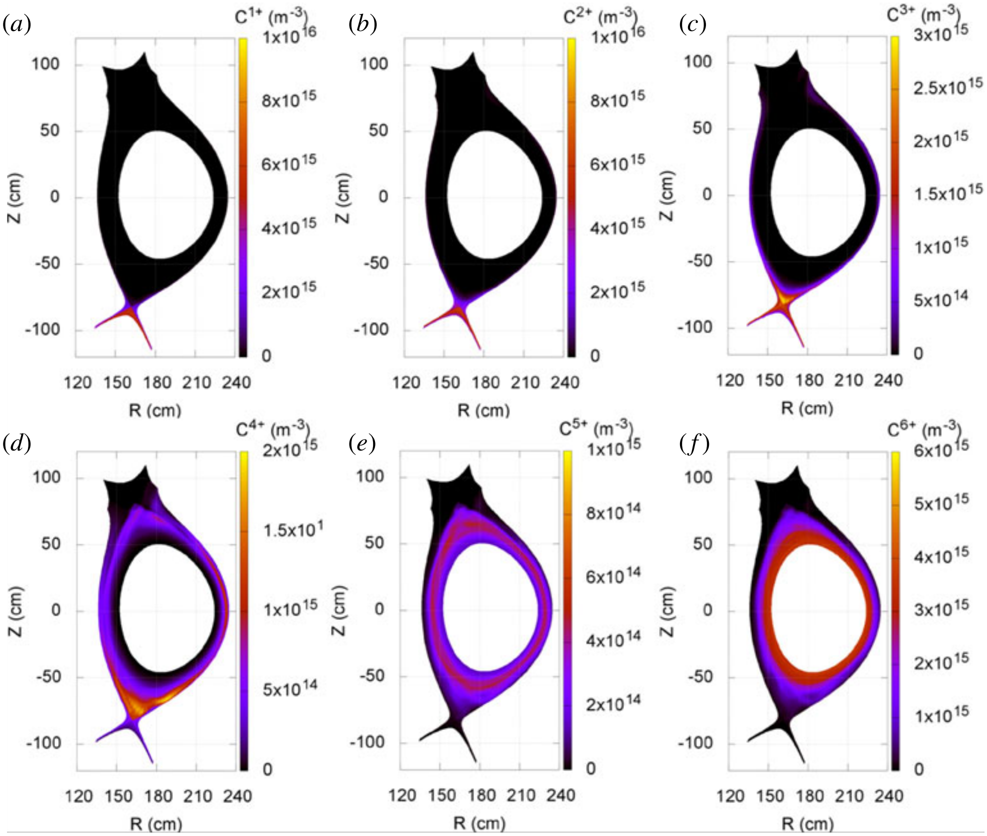

FIGURE 6. Two-dimensional distributions of C^{1+} (*a*), C^{2+} (*b*), C^{3+} (*c*), C^{4+} (*d*), C^{5+} (*e*) and C^{6+} (*f*) by EMC3-EIRENE modelling for the perturbed case at the toroidal angle of $\varphi = 56.25^\circ$.

the radial position of the resonance layer where large magnetic islands exist is mainly located at $\psi_N = 0.85–0.9$. The stronger CVI emission region ($>1 \times 10^{17}$ Photons $* \mathrm{m}^{-3} * \ \mathrm{s}^{-1}$) in figure 7 is located at the radial positions of approximately $\psi_N = 0.7–0.96$. The radial position of the resonance layer overlaps with the stronger CVI emission region. Hence, the RMP fields can affect the CVI emission distribution.

The line integration of the simulated CVI emission intensity has been performed along each observation chord to obtain the vertical profiles of the CVI emission intensity. Figure 8 shows the vertical distributions of the CVI emission intensity calculated according to EMC3-EIRENE simulation results for the perturbed and equilibrium cases at the toroidal angle of $\varphi = 56.25^\circ$. The simulated CVI emission intensity for the case with RMP fields is higher than that without RMP application, which is contrary to the experimental results in figure 3. In addition, it is seen that the CVI emissions increase along Z for the perturbed and equilibrium cases in figure 8, which is consistent with the measured CVI emission tendency in figure 3.

Due to the limited capacity of the spectroscopic diagnostics, the absolute calibration of the CVI emission cannot be performed on EAST at present. Hence, the emission intensity ratio between the RMP and no RMP cases is used to make a direct comparison between simulations and experiments. The CVI emission intensity ratio is

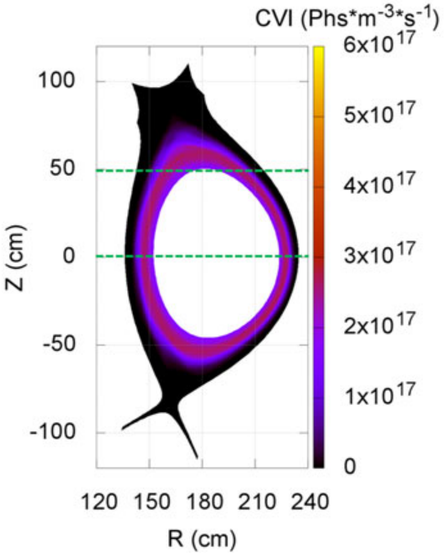

FIGURE 7. Two-dimensional distribution of the CVI emission intensity by EMC3-EIRENE modelling for the perturbed case at the toroidal angle of $\varphi = 56.25°$. The green dashed lines indicate the vertical observation range of the EUV spectrometer.

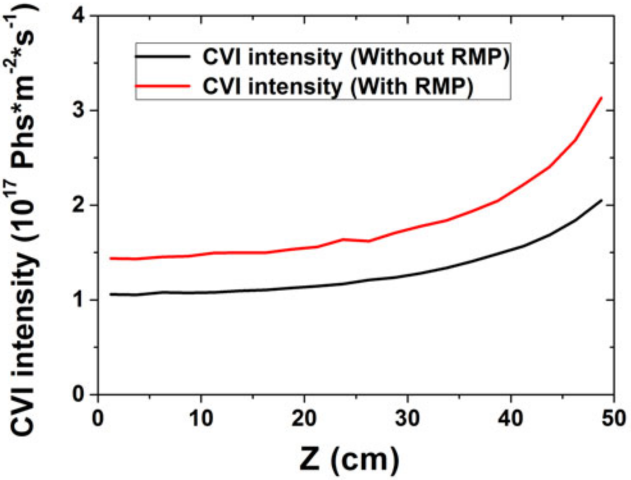

FIGURE 8. Profiles of the vertical distributions of the CVI emission intensities calculated according to EMC3-EIRENE simulation results for the cases with and without RMP applications at the toroidal angle of $\varphi = 56.25°$.

defined as the ratio of the CVI emission intensity for the perturbed case to that for the equilibrium case. Figure 9 shows the vertical distributions of the CVI emission intensity ratios between the perturbed and equilibrium cases measured by the EUV spectrometer and calculated according to EMC3-EIRENE modelling at the toroidal angle of $\varphi = 56.25°$. It is seen that the simulated CVI emission intensity ratio is higher than the measured values in the vertical observation range. The simulated CVI

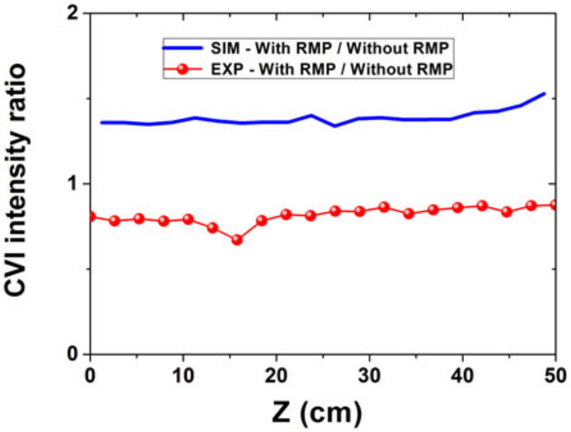

FIGURE 9. Profiles of the vertical distributions of the CVI emission intensity ratio between the perturbed and equilibrium cases measured by the EUV spectrometer and calculated according to EMC3-EIRENE modelling ($D_{\mathrm{imp}} = 0.4\ \mathrm{m^2\ s^{-1}}$) at the toroidal angle of $\varphi = 56.25^\circ$.

emission intensity ratio is approximately 1.3 in figure 9, which is more than 60 % higher than the experimental CVI emission intensity ratio (~0.8). In the following subsection, the influences of edge plasma parameters and impurity perpendicular transport on the CVI emission intensity are investigated by EMC3-EIRENE modelling to explain the difference between experiments and simulations.

5. Change of the CVI emission intensity ratio

The uncertainty in the selection of edge plasma parameters for the equilibrium case perhaps leads to the discrepancy in the CVI emission between experiments and simulations. In the modelling, the different upstream plasma densities ($n_u = 0.73 \times 10^{19}$, 0.85×10^{19} and $1.0 \times 10^{19}\ \mathrm{m^{-3}}$) are employed for the equilibrium case. Here, it is noted that the upstream plasma parameters for the perturbed case ($n_u = 0.73 \times 10^{19}\ \mathrm{m^{-3}}$, $D_\perp = 0.4\ \mathrm{m^2\ s^{-1}}$ and $\chi_\perp = 2.0\ \mathrm{m^2\ s^{-1}}$) are constant in the modelling. Figure 10 shows the vertical distributions of the CVI emission intensity ratios between the perturbed and equilibrium cases measured by the EUV spectrometer and calculated according to EMC3-EIRENE modelling at the toroidal angle of $\varphi = 56.25^\circ$ ($D_\perp = 0.4\ \mathrm{m^2\ s^{-1}}$ and $\chi_\perp = 2.0\ \mathrm{m^2\ s^{-1}}$). The CVI emission intensity is associated with the impurity density and edge plasma parameters according to (4.1). For the case of $n_u = 0.85 \times 10^{19}\ \mathrm{m^{-3}}$, the higher edge plasma density leads to a larger emission intensity, which results in the reduced CVI emission intensity ratio compared to the case of $n_u = 0.73 \times 10^{19}\ \mathrm{m^{-3}}$. However, for the case of $n_u = 1.0 \times 10^{19}\ \mathrm{m^{-3}}$, the CVI emission intensity ratio is increased compared to $n_u = 0.73 \times 10^{19}\ \mathrm{m^{-3}}$, which results in an even larger deviation from the measured values. This indicates that the CVI emission intensity for the equilibrium case is reduced for the case of $n_u = 1.0 \times 10^{19}\ \mathrm{m^{-3}}$.

The higher upstream plasma density ($n_u = 1.0 \times 10^{19}\ \mathrm{m^{-3}}$) leads to a larger D incident flux and carbon erosion on the lower divertor targets. However, the C^{5+}(CVI) density does not increase for the case of $n_u = 1.0 \times 10^{19}\ \mathrm{m^{-3}}$ as shown in figure 11, which presents the 2-D distributions of the C^{5+} (CVI) density for $n_u = 0.73 \times 10^{19}$

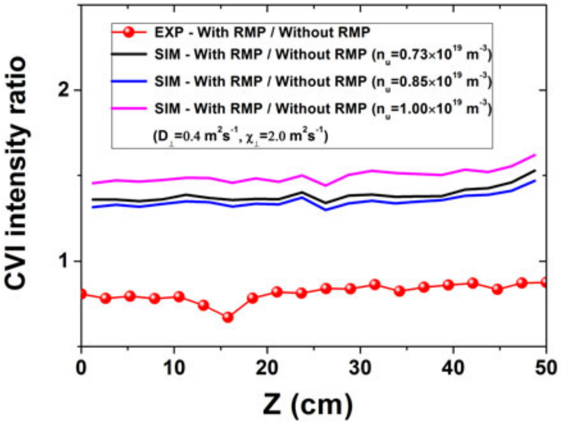

FIGURE 10. Profiles of the vertical distributions of the CVI emission intensity ratio between the perturbed and equilibrium cases measured by the EUV spectrometer and calculated according to EMC3-EIRENE modelling ($D_{\mathrm{imp}} = 0.4\ \mathrm{m}^2\ \mathrm{s}^{-1}$) at the toroidal angle of $\varphi = 56.25°$. The different upstream plasma densities ($n_u = 0.73 \times 10^{19}$, 0.85×10^{19} and $1.0 \times 10^{19}\ \mathrm{m}^{-3}$) are used for the equilibrium case ($D_\perp = 0.4\ \mathrm{m}^2\ \mathrm{s}^{-1}$ and $\chi_\perp = 2.0\ \mathrm{m}^2\ \mathrm{s}^{-1}$).

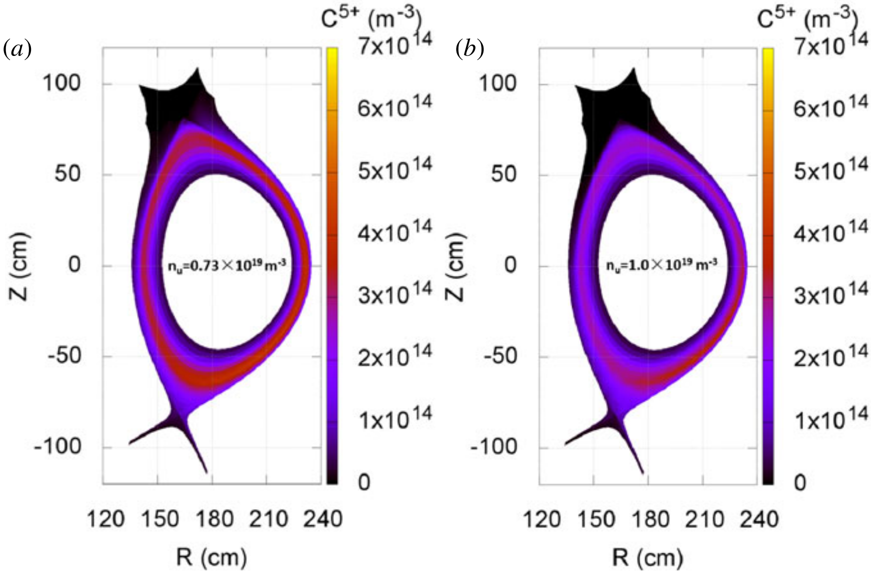

FIGURE 11. Two-dimensional distributions of C^{5+} densities for $n_u = 0.73 \times 10^{19}\ \mathrm{m}^{-3}$ (*a*) and $1.0 \times 10^{19}\ \mathrm{m}^{-3}$ (*b*) by EMC3-EIRENE modelling for the equilibrium case at the toroidal angle of $\varphi = 56.25°$.

and $1.0 \times 10^{19}\ \mathrm{m}^{-3}$ by EMC3-EIRENE modelling without RMP application at the toroidal angle of $\varphi = 56.25°$. It can be seen that the C^{5+} (CVI) density in the observation range is a little larger for $n_u = 0.73 \times 10^{19}\ \mathrm{m}^{-3}$. The small upstream plasma density leads to a higher edge plasma temperature and a lower edge plasma density for the case of $0.73 \times 10^{19}\ \mathrm{m}^{-3}$. This results in an increase of the thermal

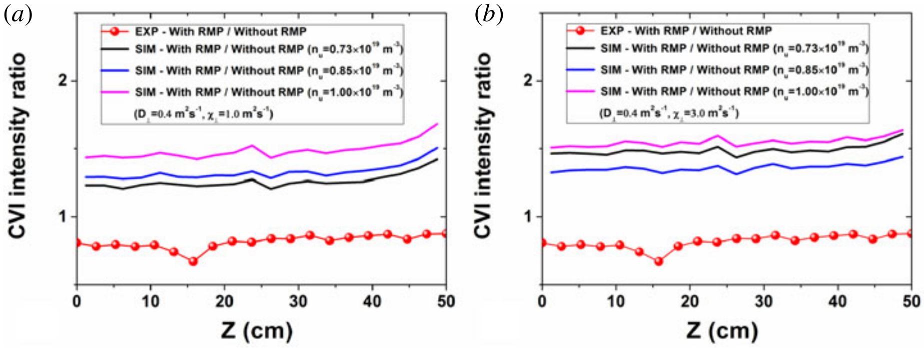

FIGURE 12. Profiles of the vertical distributions of the CVI emission intensity ratios between the perturbed and equilibrium cases measured by the EUV spectrometer and calculated according to EMC3-EIRENE modelling ($D_{\mathrm{imp}} = 0.4\ \mathrm{m^2\ s^{-1}}$) at the toroidal angle of $\varphi = 56.25^{\circ}$. The different upstream plasma densities ($n_u = 0.73 \times 10^{19}$, 0.85×10^{19} and $1.0 \times 10^{19}\ \mathrm{m^{-3}}$) are used for the equilibrium case. $D_{\perp} = 0.4\ \mathrm{m^2\ s^{-1}}$ and $\chi_{\perp} = 1.0\ \mathrm{m^2\ s^{-1}}$ for (*a*) and $D_{\perp} = 0.4\ \mathrm{m^2\ s^{-1}}$ and $\chi_{\perp} = 3.0\ \mathrm{m^2\ s^{-1}}$ for (*b*).

force and a reduction of the friction force in the edge plasma (Kobayashi *et al.* 2013*b*), which leads to a suppression of the impurity screening effect. Therefore, the larger upstream C^{5+} (CVI) density is obtained for the case of $0.73 \times 10^{19}\ \mathrm{m^{-3}}$ in figure 11 although the erosion is relatively lower. In addition, it is examined that the higher edge plasma temperature can lead to a larger emission coefficient in the simulated plasma temperature range. Both effects can offset the reduction in the edge plasma density for the case of $0.73 \times 10^{19}\ \mathrm{m^{-3}}$. Hence, the reduced CVI emission intensity is obtained for the case of $n_u = 1.0 \times 10^{19}\ \mathrm{m^{-3}}$, which results in the increased CVI emission intensity ratio for $n_u = 1.0 \times 10^{19}\ \mathrm{m^{-3}}$ in figure 10.

To further check the impacts of edge plasma parameters, different scenarios are studied in figure 12, which displays the vertical distributions of the CVI emission intensity ratios under different upstream plasma densities and plasma cross-field coefficients for the equilibrium case. It can be seen that the simulated CVI emission intensity ratios still show an obvious discrepancy from the measured values in figure 12. Since the friction force and the ion thermal force are related to the background plasma conditions, the change of edge plasma density and temperature can affect the parallel transport of carbon impurity, especially for C^{1+}–C^{4+} ions in the SOL. The change of C^{1+}–C^{4+} distributions (ionization source for C^{5+}–C^{6+}) can further have an impact on the distributions of C^{5+}–C^{6+} ions inside the perturbed separatrix. In addition, the variation of edge plasma parameters can influence the resulting carbon emission distribution according to (4.1). However, based on the simulation results in figures 10 and 12, the change of the edge plasma conditions cannot resolve the discrepancy in the CVI emission between simulations and measurements. This indicates that the uncertainty of edge plasma parameters for the equilibrium case is not responsible for the measured reduction in the CVI emission during RMP application.

In the previous simulations for LHD, it is found that the enhanced impurity perpendicular transport plays an important role in the distributions of carbon impurity density and emission (Dai *et al.* 2016*b*; Zhang *et al.* 2017). Given that the edge magnetic field structure of LHD is stochastic intrinsically, the stochastic fields induced by RMP application on EAST probably cause the enhanced perpendicular transport

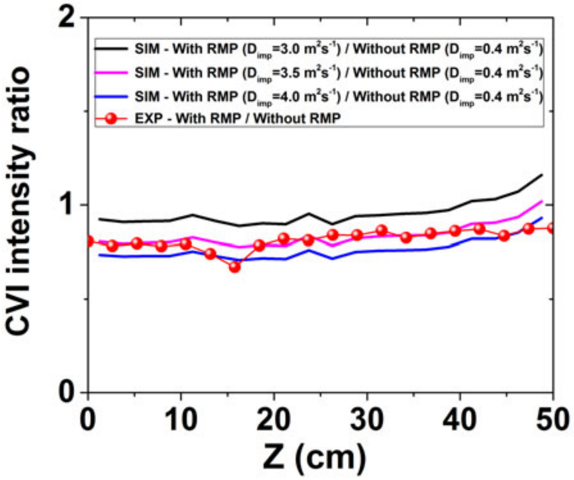

FIGURE 13. Profiles of the vertical distributions of the CVI emission intensity ratios between the perturbed and equilibrium cases measured by the EUV spectrometer and calculated according to EMC3-EIRENE modelling for different impurity perpendicular diffusivities $D_{\mathrm{imp}} = 3.0$, 3.5 and 4.0 $\mathrm{m}^2\ \mathrm{s}^{-1}$ for the perturbed case at the toroidal angle of $\varphi = 56.25^\circ$.

for the carbon impurity as well. Figure 13 shows the vertical distributions of the CVI emission intensity ratios between the perturbed and equilibrium cases measured by the EUV spectrometer and calculated according to EMC3-EIRENE modelling for different impurity perpendicular diffusivities $D_{\mathrm{imp}} = 3.0$, 3.5 and 4.0 $\mathrm{m}^2\ \mathrm{s}^{-1}$ at the toroidal angle of $\varphi = 56.25^\circ$. For the equilibrium case, the impurity perpendicular diffusivity $D_{\mathrm{imp}} = 0.4\ \mathrm{m}^2\ \mathrm{s}^{-1}$ is used. It is found that the enhanced perpendicular transport diffusivity can effectively resolve the discrepancy in the CVI emission between simulations and the measurements. It is also examined that the variation of D_{imp} does not have an impact on the plasma parameters. Hence, the change of the CVI emission against D_{imp} in the EUV observation range is mainly induced by the variation of the C^{5+} (CVI) ion density distribution according to the (4.1).

The 2-D distribution of the CVI emission intensity for the perturbed case with $D_{\mathrm{imp}} = 3.5\ \mathrm{m}^2\ \mathrm{s}^{-1}$ at the toroidal angle of $\varphi = 56.25^\circ$ is presented in figure 14. The peak value of the CVI emission for $\mathrm{D}_{\mathrm{imp}} = 3.5\ \mathrm{m}^2\ \mathrm{s}^{-1}$ is much lower than that for $D_{\mathrm{imp}} = 0.4\ \mathrm{m}^2\ \mathrm{s}^{-1}$ in figure 7. This indicates that the loss of the C^{5+} (CVI) inside the perturbed separatrix is stronger than the C^{5+} (CVI) ionization source from the penetration of C^{4+} ions for the cases with increased D_{imp}. As a result, the line-integrated CVI emission intensity ratio decreases obviously in figure 13.

Overall, the above analysis shows that the perpendicular transport of carbon impurity plays an important role in resolving the discrepancy between simulations and measurements. The observed 20 % reduction in the CVI emission for the perturbed case can be reproducible with higher D_{imp} in the modelling. While there are still some issues that need to be addressed in future work. The plasma response effects after RMP application probably lead to a modification of the edge magnetic configuration, which could have an impact on the edge impurity transport and resulting emission. Inclusion of plasma response effects will be the focus of future modelling. In addition, if the core impurity transport is solved self-consistently, the population of C^{5+} and C^{6+} may change inside the perturbed separatrix, which perhaps affects the simulated

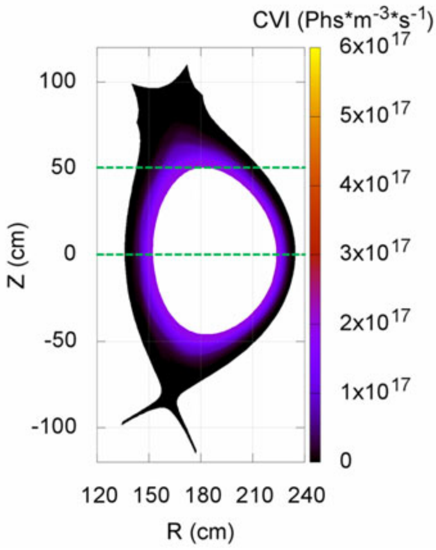

FIGURE 14. Two-dimensional distribution of the CVI emission intensity by EMC3-EIRENE modelling for the perturbed case with $D_{\mathrm{imp}} = 3.5\ \mathrm{m}^2\ \mathrm{s}^{-1}$ at the toroidal angle of $\varphi = 56.25^\circ$. The green dashed lines indicate the vertical observation range of the EUV spectrometer.

line-integrated CVI distribution. The contribution of core impurity transport has been neglected so far due to the limited capability of the simulation code. A self-consistent treatment of the entire impurity transport from the core to the edge is left for future work. There also exist uncertainties in the selection of the same carbon sputtering coefficient for the equilibrium and perturbed cases in the modelling. The sputtering coefficient may be different for the equilibrium and perturbed cases during discharge in light of the intricate wall condition and plasma–wall interactions. Accordingly, the variation of carbon impurity source after RMP application would change the simulated CVI distribution. Hence, the measurements of the sputtering source and carbon emissions in low charge states under RMP fields should be carried out to provide more experimental data for future modelling. The present analysis will be revisited with the improved model and data, which can enable us to assess further details of the impurity transport process under RMP application.

6. Summary

The transport characteristics of edge carbon impurity in the scrape-off layer of the EAST tokamak under application of RMP fields have been studied with the EMC3-EIRENE code in comparison with the EUV emission measurements. The work has been motivated to investigate the impacts of the RMP fields on edge impurity transport and emission on tokamaks compared to the axisymmetric magnetic configuration. The CVI (33.7 Å) emissions for the perturbed and equilibrium cases are measured by the EUV spectrometer system on EAST, which shows that the RMP fields can lead to a 20 % reduction in the CVI emission compared to the no RMP case. The basic characteristics of carbon impurity distribution are investigated by EMC3-EIRENE simulations for the perturbed case. The lower charge states carbon impurity (C^{1+}–C^{3+}) mainly populate at the lower divertor legs and X-point regions. The C^{4+} ions are mainly in the SOL region and C^{5+}–C^{6+} ions are inside the perturbed separatrix, respectively.

The increased CVI emission intensity is obtained by EMC3-EIRENE modelling for the perturbed case compared to the equilibrium case, which is contrary to the experimental measurements. The change of the edge plasma conditions for the equilibrium case cannot resolve the discrepancy in the CVI emission between simulations and measurements. For the high upstream plasma density, the difference in the simulated CVI emission intensities between the perturbed and equilibrium cases becomes even larger compared to the measured values. Hence, the uncertainty of edge plasma parameters for the equilibrium case is irrelevant for the interpretation of the observed reduction of CVI emission during RMP application. The impacts of the impurity perpendicular transport on the CVI emission are investigated. The simulations carried out at higher impurity perpendicular diffusivities after RMP application render a better agreement between the modelling and the experiments.

Acknowledgements

This work supported by National MCF Energy R&D Program of China Nos: 2018YFE0311100, 2018YFE0303105, 2017YFE0300501, 2017YFE0301206, 2017YFE0300402 and 2017YFE0301300, National Natural Science Foundation of China under grant nos 11675037, 11405021 and 11805231, High-level talent innovation support program of Dalian No. 2017RQ052, and the Fundamental Research Funds for the Central Universities No. DUT18LK03. The contribution by H.M.Z. was also supported by CASHIPS Director's Fund No. YZJJ201612, ASIPP Science foundation No. DSJJ-17-03, Anhui Provincial Natural Science Foundation No. 1808085QA14.

REFERENCES

BAZYLEV, B. *et al.* 2009 Experimental validation of 3D simulations of tungsten melt erosion under ITER-like transient loads. *J. Nucl. Mater.* **390–391**, 810.

BURRELL, K. H. *et al.* 2005 ELM suppression in low edge collisionality H-mode discharges using $n = 3$ magnetic perturbations. *Plasma Phys. Control. Fusion* **47**, B37.

DAI, S. Y. *et al.* 2015 Kinetic modelling of material erosion and impurity transport in edge localized modes in EAST. *Nucl. Fusion* **55**, 043003.

DAI, S. Y. *et al.* 2016*a* EMC3-EIRENE simulation of impurity transport in comparison with EUV emission measurements in the stochastic layer of LHD: effects of force balance and transport coefficients. *Contrib. Plasma Phys.* **56**, 628–633.

DAI, S. Y. *et al.* 2016*b* EMC3-EIRENE modelling of edge impurity transport in the stochastic layer of the large helical device compared with extreme ultraviolet emission measurements. *Nucl. Fusion* **56**, 066005.

DAI, S. Y. *et al.* 2018 Three-dimensional simulations of edge impurity flow obtained by the vacuum ultraviolet emission diagnostics in the Large Helical Device with EMC3-EIRENE. *Nucl. Fusion* **58**, 096024.

ECKSTEIN, W. 2008 Sputtering yields. *Vacuum* **82**, 930.

EICH, T. *et al.* 2005 Power deposition onto plasma facing components in poloidal divertor tokamaks during type-I ELMs and disruptions. *J. Nucl. Mater.* **337–339**, 669.

EVANS, T. E. *et al.* 2004 Suppression of large edge-localized modes in high-confinement DIII-D plasmas with a stochastic magnetic boundary. *Phys. Rev. Lett.* **92**, 235003.

EVANS, T. E. *et al.* 2005 Experimental signatures of homoclinic tangles in poloidally diverted tokamaks. *J. Phys. Conf. Ser.* **7**, 174.

EVANS, T. E. *et al.* 2006 Edge stability and transport control with resonant magnetic perturbations in collisionless tokamak plasmas. *Nat. Phys.* **2**, 419.

EVANS, T. E. *et al.* 2013 ELM mitigation techniques. *J. Nucl. Mater.* **438**, S11–S18.

FAITSCH, M. *et al.* 2017 2D heat flux in ASDEX Upgrade L-Mode with magnetic perturbation. *Nucl. Mater. Energy* **12**, 1020.

FEDERICI, G. *et al.* 2001 Plasma-material interactions in current tokamaks and their implications for next step fusion reactors. *Nucl. Fusion* **41**, 1967.

FEDERICI, G. *et al.* 2003 Assessment of erosion of the ITER divertor targets during type I ELMs. *Plasma Phys. Control. Fusion* **45**, 1523.

FENG, Y. *et al.* 2002 Transport in island divertors: physics, 3D modelling and comparison to first experiments on W7-AS. *Plasma Phys. Control. Fusion* **44**, 611.

FENG, Y. *et al.* 2004 3D edge modeling and island divertor physics. *Contrib. Plasma Phys.* **44**, 57.

FENG, Y. *et al.* 2005 A simple highly accurate field-line mapping technique for three-dimensional Monte Carlo modeling of plasma edge transport. *Phys. Plasmas* **12**, 052505.

FENG, Y. *et al.* 2017 Monte-Carlo fluid approaches to detached plasmas in non-axisymmetric divertor configurations. *Plasma Phys. Control. Fusion* **59**, 034006.

FRERICHS, H. *et al.* 2010 Block-structured grids in Lagrangian 3D edge plasma transport simulations. *Comput. Phys. Commun.* **181**, 61–70.

FRERICHS, H. *et al.* 2012*a* On gas flow effects in 3D edge transport simulations for DIII-D plasmas with resonant magnetic perturbations. *Nucl. Fusion* **10**, 054008.

FRERICHS, H. *et al.* 2012*b* Impact of screening of resonant magnetic perturbations in three dimensional edge plasma transport simulations for DIII-D. *Phys. Plasmas* **19**, 052507.

FRERICHS, H. *et al.* 2013 Numerical sensitivity analysis of divertor heat flux and edge temperature at DIII-D under the influence of resonant magnetic perturbations. *J. Nucl. Mater.* **438**, S360–S363.

FRERICHS, H. *et al.* 2014 Striation pattern of target particle and heat fluxes in three dimensional simulations for DIII-D. *Phys. Plasmas* **21**, 020702.

FRERICHS, H. *et al.* 2016*a* Exploration of magnetic perturbation effects on advanced divertor configurations in NSTX-U. *Phys. Plasmas* **23**, 062517.

FRERICHS, H. *et al.* 2016*b* Synthetic plasma edge diagnostics for EMC3-EIRENE, highlighted for Wendelstein 7-X. *Rev. Sci. Instrum.* **87**, 11D441.

FRERICHS, H. *et al.* 2017 Reconstruction of recycling flux from synthetic camera images, evaluated for the Wendelstein 7-X startup limiter. *Nucl. Fusion* **57**, 126022.

HUANG, J. *et al.* 2014 Implementation and first application of EMC3-EIRENE to EAST double-null divertor. *Plasma Phys. Control. Fusion* **56**, 075023.

JEON, Y. M. *et al.* 2012 Suppression of edge localized modes in high-confinement KSTAR plasmas by nonaxisymmetric magnetic perturbations. *Phys. Rev. Lett.* **109**, 035004.

JIA, M. N. *et al.* 2016 Vacuum modeling of three-dimensional magnetic field topology under resonant magnetic perturbations on EAST. *Plasma Phys. Control. Fusion* **58**, 055010.

JIA, M. N. *et al.* 2018*a* Control of three dimensional particle flux to divertor using rotating RMP in the EAST tokamak. *Nucl. Fusion* **58**, 046015.

JIA, M. N. *et al.* 2018*b* Dynamic divertor control using resonant mixed toroidal harmonic magnetic fields during ELM suppression in DIII-D. *Phys. Plasmas* **25**, 056102.

KAWAMURA, G. *et al.* 2018 Three-dimensional impurity transport modeling of neon-seeded and nitrogen-seeded LHD plasmas. *Plasma Phys. Control. Fusion* **60**, 084005.

KIRK, A. *et al.* 2010 Resonant magnetic perturbation experiments on MAST using external and internal coils for ELM control. *Nucl. Fusion* **50**, 034008.

KOBAYASHI, M. *et al.* 2008 Modelling of impurity transport in ergodic layer of LHD. *Contrib. Plasma Phys.* **48**, 255–259.

KOBAYASHI, M. *et al.* 2009 Model prediction of impurity retention in stochastic magnetic boundary and comparison with edge carbon emission in LHD. *J. Nucl. Mater.* **390–391**, 325–329.

KOBAYASHI, M. *et al.* 2010 Detachment stabilization with $n/m = 1/1$ resonant magnetic perturbation field applied to the stochastic magnetic boundary of the large helical device. *Phys. Plasmas* **17**, 056111.

KOBAYASHI, M. *et al.* 2013*a* Control of 3D edge radiation structure with resonant magnetic perturbation fields applied to the stochastic layer and stabilization of radiative divertor plasma in LHD. *Nucl. Fusion* **53**, 093032.

KOBAYASHI, M. *et al.* 2013*b* Edge impurity transport study in the stochastic layer of LHD and the scrape-off layer of HL-2A. *Nucl. Fusion* **53**, 033011.

KOBAYASHI, M. *et al.* 2017 2D distribution of hydrogen/impurity radiation and flow formation in stochastic layer during detachment transition in LHD. *Nucl. Mater. Energy* **12**, 1043.

KOBAYASHI, M. *et al.* 2019 Impact of a resonant magnetic perturbation field on impurity radiation, divertor footprint, and core plasma transport in attached and detached plasmas in the large helical device. *Nucl. Fusion* **59**, 096009.

LANG, P. T. *et al.* 2013*a* ELM pacing and trigger investigations at JET with the new ITER-like wall. *Nucl. Fusion* **53**, 073010.

LANG, P. T. *et al.* 2013*b* ELM control strategies and tools: status and potential for ITER. *Nucl. Fusion* **53**, 043004.

LAO, L. L. *et al.* 1990 Equilibrium analysis of current profiles in tokamaks. *Nucl. Fusion* **30**, 1035.

LIANG, Y. F. *et al.* 2007 Active control of type-I edge-localized modes with $n = 1$ perturbation fields in the JET tokamak. *Phys. Rev. Lett.* **98**, 265004.

LOARTE, A. *et al.* 2007 Progress in the ITER physics basis, chapter 4: power and particle control. *Nucl. Fusion* **47**, S203.

LOARTE, A. *et al.* 2014*a* Evolution of plasma parameters in the termination phase of high confinement H-modes at JET and implications for ITER. *Nucl. Fusion* **54**, 123014.

LOARTE, A. *et al.* 2014*b* Progress on the application of ELM control schemes to ITER scenarios from the non-active phase to DT operation. *Nucl. Fusion* **54**, 033007.

LORE, J. D. *et al.* 2012 Implementation of the 3D edge plasma code EMC3-EIRENE on NSTX. *Nucl. Fusion* **52**, 054012.

LORE, J. D. *et al.* 2017 Pedestal-to-wall 3D fluid transport simulations on DIII-D. *Nucl. Fusion* **57**, 056025.

LUNT, T. *et al.* 2012 First EMC3-Eirene simulations of the impact of the edge magnetic perturbations at ASDEX Upgrade compared with the experiment. *Nucl. Fusion* **52**, 054013.

OISHI, T. *et al.* 2018 Observation of carbon impurity flow in the edge stochastic magnetic field layer of Large Helical Device and its impact on the edge impurity control. *Nucl. Fusion* **58**, 016040.

RAPP, J. *et al.* 2009 Integrated scenario with type-III ELMy H-mode edge: extrapolation to ITER. *Nucl. Fusion* **49**, 095012.

REITER, D. *et al.* 2005 3D edge modeling and island divertor physics. *Fusion Sci. Technol.* **47**, 172.

SCHMITZ, O. *et al.* 2013 Modeling of divertor particle and heat loads during application of resonant magnetic perturbation fields for ELM control in ITER. *J. Nucl. Mater.* **438**, S194–S198.

SCHMITZ, O. *et al.* 2014 Formation of a three-dimensional plasma boundary after decay of the plasma response to resonant magnetic perturbation fields. *Nucl. Fusion* **54**, 012001.

SCHMITZ, O. *et al.* 2016 Three-dimensional modeling of plasma edge transport and divertor fluxes during application of resonant magnetic perturbations on ITER. *Nucl. Fusion* **56**, 066008.

SHEN, Y. C. *et al.* 2013 Space-resolved extreme ultraviolet spectrometer system for impurity behavior research on experimental advanced superconducting Tokamak. *Nucl. Instr. Meth. Phys. Res.* A **700**, 86–90.

STANGEBY, P. C. 2000 *The Plasma Boundary of Magnetic Fusion Devices*. Institute of Physics Publishing.

SUN, Y. W. *et al.* 2016 Nonlinear transition from mitigation and suppression of the edge localized mode with resonant magnetic perturbations in the EAST tokamak. *Phys. Rev. Lett.* **117**, 115001.

SUN, Y. W. *et al.* 2017 Edge localized mode control using $n = 1$ resonant magnetic perturbation in the EAST tokamak. *Nucl. Fusion* **57**, 036007.

SUTTROP, W. *et al.* 2011 First observation of edge localized modes mitigation with resonant and nonresonant magnetic perturbations in ASDEX Upgrade. *Phys. Rev. Lett.* **106**, 225004.

TEMMERMAN, G. D. *et al.* 2011 ELM simulation experiments on Pilot-PSI using simultaneous high flux plasma and transient heat/particle source. *Nucl. Fusion* **51**, 073008.

VOGEL, G. *et al.* 2018 Extreme ultraviolet spectroscopy applied to study RMP effects on core impurity concentration in EAST. *IEEE T Plasma Sci.* **46**, 1350.

XIE, T. *et al.* 2018*a* Investigation of edge impurity transport derived from the first wall on EAST with EMC3-EIRENE modelling. *Fusion Engng Des.* **136**, 699–705.

XIE, T. *et al.* 2018*b* EMC3-EIRENE modelling of edge plasma and impurity emissions compared with the liquid lithium limiter experiment on EAST. *Nucl. Fusion* **58**, 106017.

ZHANG, H. M. *et al.* 2017 Vertical profiles and two-dimensional distributions of carbon line emissions from C^{2+}–C^{5+} ions in attached and RMP-assisted detached plasmas of large helical device. *Phys. Plasmas* **24**, 022510.